A sustainable carbon-consuming cycle based on sequential activation of CO_2 and CH_4 using metal oxides

Seungdon Kwon [a], Hyogeun Yang [a], Youngjae Yu [a], Yuyeol Choi [a], Nagyeong Kim [a], Gye Hong Kim [b], Kyoung Chul Ko [c], Kyungsu Na [a,*]

[a] *Department of Chemistry, Chonnam National University, Gwangju 61186, the Republic of Korea*
[b] *Department of Earth Systems and Environmental Sciences, Chonnam National University, Gwangju 61186, the Republic of Korea*
[c] *Department of Chemistry Education, Chonnam National University, Gwangju 61186, the Republic of Korea*

A B S T R A C T

Naturally abundant metal oxides can be used as reusable CO_2-philic absorbents, and the resulting CO_2-bound metal carbonates are disposed in nature; although common, this carbon capture and sequestration process is unsustainable. Herein, we revisit the use of metal carbonates as pre-activated CO_2 reservoir containing reactive carbonate species that can combine with CH_4 to produce CH_3COOH. The direct stoichiometric coupling of CH_4 with CO_2 to form CH_3COOH is thermodynamically non-spontaneous. However, theoretical calculations identified metal carbonates that spontaneously react with CH_4 to form CH_3COOH and the corresponding metal oxides. We designed new metal oxide-assisted carbon-consuming cycle involving sequential CO_2/CH_4 activation to form CH_3COOH with nearly 100% selectivity, which can be generalized to various metal oxides. Particularly, Co_3O_4 nanoparticles encapsulated by mesoporous silica shell produced the best CH_3COOH productivity of 0.7 $\mu mol_{CH3COOH}$ g_{Co3O4}^{-1} at 250 °C, which enables the sustainable incremental production of CH_3COOH without decrease in productivity over 15 repeated cycles.

1. Introduction

Industrial revolution improved the quality of life, but it came at the expense of higher global temperatures due to its dependence on fossil fuel energy, resulting in the emission of several billion tons of CO_2 that pose a serious threat to human life [1]. Without a sharp transition to a fossil fuel-free society and industry, achieving an environment-friendly sustainable growth is impossible. The ultimate solution for reducing the CO_2 concentration in the atmosphere should be the elimination of CO_2-emitting processes; however, this could only be realized by ending most industrial processes that support the current society [1]. A possible compromise involves CO_2 capture from the emission source before it reaches the atmosphere, using CO_2-philic materials such as metal oxides, followed by sequestration of the CO_2-bound metal carbonates deep underground or under the sea [2–5]. However, such CO_2 capture and sequestration (CCS) technologies cause acidification of terrestrial and marine environments, which is detrimental to the ecosystem and hence not sustainable [2–5]. A potential solution that has been investigated for several decades could be employing CO_2 for manufacturing value-added

chemicals through little energy input, ideally provided by renewable sources [6–12]. However, only few of them were industrialized [9–12]; one example is the CO_2 cycloaddition to epoxide for the synthesis of organic cyclic carbonates that can be used as electrolytes in batteries or as monomers in polycarbonate syntheses [12–14]. Interestingly, the formation of organic cyclic carbonates may be considered a nature-mimetic chemical process, reminiscent of the spontaneous CO_2 mineralization in metal oxides to form metal carbonates. However, there is still a long journey toward the practical and sustainable utilization of CO_2, which is hindered by the high inertness of CO_2, whose activation requires overcoming a high energy barrier using powerful catalysts [15].

Similar to CO_2, CH_4 is another member of the C_1 family including other oxygenated compounds (CO, CO_2, CH_2O, CH_3OH) [16–20]; methane is the lightest fully saturated hydrocarbon possessing stable C–H bonds with high dissociation energy (*ca.* 439 kJ mol^{-1}) [16] and is considered a greenhouse gas with approximately 21 times higher global warming potential than CO_2 [20]. The shale revolution resulted in the dramatic growth of CH_4 mining [21–23], which led worldwide scientists to pioneer newer and more sustainable routes for CH_4 utilization

---

[21–26]. Although CH_4 can be used directly as fuel [20], catalytic CH_4 conversion to various products *via* cracking, partial oxidation, halogenation, dehydroaromatization, and oxidative/non-oxidative coupling can add value to CH_4 compared to merely using it as combustible fuel [17–20,23–30]. CH_4 can react with CO_2 to produce the utilizable syngas mixture $CO + H_2$ *via* dry reforming of methane (Eq. 1) [26], but this process is still impractical, owing to its highly endothermic nature that consumes tremendous amounts of energy and severely damages the catalysts, resulting in their deactivation during the reaction [26]. Alternatively, both greenhouse gases can be combined in one-to-one molar ratio, producing an equimolar amount of CH_3COOH, which is an important organic acid in industry (Eq. 2) [27–30]. Although this reaction appears as atom-economic, it is a non-spontaneous process, owing to its large positive Gibbs energy (ΔG) values under industrial operating conditions of temperature and pressure (Fig. S1) [29,30]. Currently, CH_3COOH is mainly manufactured *via* methanol carbonylation with CO (Monsanto or Cativa processes) using organometallic compounds as homogeneous catalysts [31–33].

$$CH_4 \text{ (g)} + CO_2 \text{ (g)} \rightarrow 2CO \text{ (g)} + 2H_2 \text{ (g)} \tag{1}$$

$$CH_4 \text{ (g)} + CO_2 \text{ (g)} \rightarrow CH_3COOH \text{ (g)} \tag{2}$$

$$MCO_3 \text{ (s)} + CH_4 \text{ (g)} \rightarrow MO \text{ (s)} + CH_3COOH \text{ (g)} \tag{3}$$
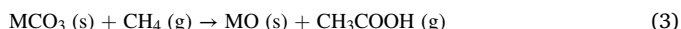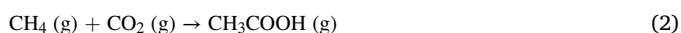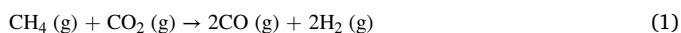
Herein, we developed a new route for CH_4 conversion to CH_3COOH, in which a metal carbonate provides pre-activated CO_2 that can react with CH_4. In the free molecular state, CO_2 has a large bandgap energy (E_g) for activation (Fig. S2), and its direct coupling with CH_4 to form CH_3COOH presents large positive ΔG values at various pressures and temperatures, indicating a non-spontaneous reaction (Fig. S1). Owing to the high E_g values of both CH_4 and CO_2, their electronic activations are very difficult, which prevents their coupling to form the desired compound, *i.e.*, CH_3COOH (Fig. S2). In contrast, the carbonate ion (CO_3^{2-}) has a narrower E_g; hence, activating it in metal carbonates would be easier than activating the free CO_2 molecule (Fig. S2). The reaction between CH_4 and the metal carbonates was selected based on the fact that the vibrational energy of CO_2 bound in CO_3^{2-} form on the metal oxide surface increases upon elevation of the temperature, releasing CO_2 from the metal carbonates. As the applied temperature increases, the vibrations of CO_2 bound in carbonate form in the metal carbonate framework become more intense, finally releasing CO_2 as a free molecule. We assumed that the vibrating CO_2 in the carbonate species possesses higher reactivity than the free CO_2 molecule, which would enable the reaction with CH_4 if the latter is also activated in proximity to the vibrating CO_2. We prescreened the reaction spontaneity using theoretical phonon calculations to derive the ΔG values for the reaction between various metal carbonates (MCO_3) and CH_4 to produce metal oxides (MO) and CH_3COOH (Eq. 3); this allows us to identify potential metal carbonate candidates that would make the reaction in Eq. 3 feasible.

2. Experimental

2.1. Computational detail

To determine the experimental conditions for which the forward reaction in Eq. 3 is spontaneous, we calculated the Gibbs free energy changes (ΔG) for reaction in Eq. 3 [metal carbonate (MCO_3, s) + CH_4 (g) → metal oxide (MO, s) + CH_3COOH (g)], in terms of translation, rotational, and vibrational partition functions based on the density functional theory (DFT) method. Detailed DFT calculations were explained in the Supplementary Material.

2.2. Materials synthesis

2.2.1. Chemicals

All chemicals employed in this study were commercially available and used as received without any other purification. As commercially available metal carbonates, cobalt carbonate basic (($CoCO_3$)$_2$·[Co$(OH)_2$]$_3$, extra-pure), copper carbonate basic ($CuCO_3$·$Cu(OH)_2$, chemically pure), and zinc carbonate basic [($ZnCO_3$)$_2$·[$Zn(OH)_2$]$_3$, chemically pure] were purchased from DAEJUNG Chemical for reaction studies. Cobalt oxide (Co_3O_4) was purchased from Sigma-Aldrich in bulk structure, denoted as bCo_3O_4.

2.2.2. Synthesis of nCo_3O_4

The nanostructured Co_3O_4, denoted as nCo_3O_4, was prepared *via* the co-precipitation method using the procedures described below. A 62.27 g amount of cobalt acetate tetrahydrate [$(CH_3COO)_2Co$•4 H_2O, extra-pure, DAEJUNG] was dissolved in 1 L of distilled water to obtain a concentration of 0.25 M. After the solution was heated to 70 °C, 250 mL of aqueous ammonia solution (25% NH_3, extra-pure, DAEJUNG) was added and stirred for 1 h. The resulting solution was cooled to 25 °C, and a light pink precipitate was collected by centrifugation and thoroughly washed with distilled water. The precipitated solid was dried in a vacuum oven at 60 °C for 6 h. The dried powder was calcined in a furnace at 200 °C for 6 h under air with a flow rate of 100 cm^3 min^{-1}.

2.2.3. Synthesis of $nCo_3O_4@mSiO_2$

Co_3O_4 nanoparticles encapsulated by mesoporous silica with nanosponge-type structure, denoted as $nCo_3O_4@mSiO_2$, were prepared following modified procedures reported in the literature, as described below [34–36]. A 0.55 g amount of cobalt nitrate hexahydrate (Co$(NO_3)_2$·$6H_2O$, extra-pure, DAEJUNG) and 1.75 g of polyvinylpyrrolidone (M_w ~55000, Sigma-Aldrich) was dissolved in 120 mL of absolute ethanol, stirred at 25 °C for 1 h, heated in a Teflon-lined stainless steel autoclave at 180 °C, and maintained at that temperature for 5 h. The resulting black colloidal solution was added to a solution containing 0.62 g of cetyltrimethylammonium bromide (99%, DAEJUNG) and 63.5 mL of aqueous ammonia solution (25%) in 400 mL mixed solution of ethanol and distilled water (3:2 v/v). Then, 1.95 g of tetraethyl orthosilicate (98%, Sigma-Aldrich) was added to this solution and stirred at 25 °C for 2 days. The solid product was filtered, washed with distilled water and absolute ethanol, dried at 80 °C for 12 h, and calcined in a furnace at 550 °C for 6 h under air with a flow rate of 100 cm^3 min^{-1}.

2.3. Materials characterization

Thermogravimetric analysis with differential scanning calorimetry (TGA–DSC) was performed using a STA 6000 instrument (PerkinElmer). The sample was heated by increasing the temperature of the cell from 50° to 800°C at a ramping rate of 5 °C min^{-1} under N_2 atmosphere, and kept at 800 °C for 30 min. X-ray diffraction (XRD) patterns were recorded using a Rigaku MiniFlex 600 instrument with a Cu tube with K_α radiation ($\lambda = 0.1541$ nm) operated at 600 W (40 kV, 15 mA). The measurements were performed under ambient conditions using a step size of 0.005°, a scanning rate of 3° min^{-1}, and a 2θ range of 20–70 °. Fourier transform infrared (FT-IR) spectra were obtained using a Nicolet iS50R spectrometer (Thermo Fisher Scientific Inc.) equipped with a mercury–cadmium–telluride detector in attenuated total reflection (ATR) mode using a ZnSe crystal (Pike MIRacle). The measurements were carried out with an average of 64 scans in the range of 650–4000 cm^{-1}, with a data interval of 0.482 cm^{-1} and a resolution of 4 cm^{-1}. All FT-IR spectra were recorded at room temperature in an air-conditioned room. N_2 physisorption analysis was performed using a BELSORP MAX II volumetric analyzer at liquid N_2 temperature (77 K). Prior to the measurements, samples were degassed at 150 °C under vacuum for 3 h. Specific surface areas and pore sizes were calculated

according to the Brunauer–Emmett–Teller (BET) and Barrett–Joyner–Halenda (BJH) methods, respectively. Crystal morphologies were examined *via* transmission electron microscopy–energy dispersive X-ray spectroscopy (TEM–EDS). TEM and EDS elemental mapping images were collected using a JEM-2100 F (JEOL Ltd.) instrument operating at 200 kV and an Optima 8300 spectrometer (PerkinElmer). Elemental contents were analyzed using inductively coupled plasma–optical emission spectroscopy (ICP-OES, OPTIMA 8500, PerkinElmer Inc.).

2.4. Reaction study

2.4.1. Continuous flow fixed-bed reaction

A continuous flow fixed-bed reaction using metal carbonate and CH_4 was conducted in a 0.5-inch-diameter microreactor made with Inconel alloys. The reaction was carried out in the temperature range of 150–350 °C under pressurized conditions with pure CH_4 gas, and the gas flow rate was controlled using a mass flow controller (LineTech). The temperature of the reactor was monitored using a thermocouple located inside the sample bed. In a typical reaction process, the metal carbonate was sieved through a 20–40 mesh and placed inside the fixed-bed microreactor. Prior to the reaction, the microreactor was purged with N_2 at a flow rate of 10 cm^3 min^{-1}, while the temperature was increased to the target value. Then, CH_4 was fed at a flow rate of 5 cm^3 min^{-1} until the reactor was pressurized to 20 bar. After reaching the target pressure, the CH_4 flow was kept for 2 h. The outlet stream was kept at 200 °C to avoid the condensation of the gaseous products before they reached the cold trap filled with ethanol. The cold trap was kept at 5 °C by using ice jacket. The products were analyzed using a gas chromatograph (GC) equipped with a flame-ionization detector (FID), thermal conductivity detector (TCD), and a capillary column (HP-FFAP, 30 m length, 0.53 mm diameter, 1 μm thickness). The detection limit of product is approximately 10 nmol scale, under which product cannot be distinguished from noise in the GC-FID chromatogram.

2.4.2. Stepwise CO_2 and CH_4 feeding reaction

A stepwise CO_2 and CH_4 feeding reaction was conducted in the same microreactor described above. The reaction was investigated at 250 °C and 20 bar, with a stepwise feeding of CO_2 and CH_4 to the reactor containing the metal oxide materials purchased or synthesized in this work. In a typical cycle reaction process, the metal oxides were used as a 20–40 mesh sieve that was placed inside the fixed-bed microreactor. Prior to the reaction, the microreactor was purged with N_2 at a flow rate of 10 cm^3 min^{-1} while the temperature was increased to 250 °C. The N_2 gas was switched to CO_2 with a flow rate of 5 cm^3 min^{-1} until the reactor was pressurized to 20 bar. After the target pressure was reached, the CO_2 flow was kept for 10 min and then decompressed to 1 bar. The CO_2 gas was switched to CH_4 with a flow rate of 5 cm^3 min^{-1} until the reactor was pressurized to 20 bar. After the target pressure was reached, the CH_4 flow was kept for 10 min and then decompressed to 1 bar. Subsequently, the CH_4 gas was switched to N_2 gas with a flow rate of 10 cm^3 min^{-1} to purge the products, which were collected in a cold trap containing ethanol for condensation. The complete reaction cycle was repeated 15 times.

3. Results and discussion

3.1. Computational screening of metal carbonates for CH_4 conversion to CH_3COOH

Phonon calculations were carried out for various metal carbonates (Figs. S3 and S4); the results revealed that some metal carbonates exhibited negative ΔG regions for the forward reaction in Eq. 3. Among the investigated metal carbonates, $CoCO_3$, $CuCO_3$, and $ZnCO_3$ exhibited a spontaneous forward reaction in the negative ΔG regions above 994, 267, and 800 K, respectively (Figs. S3 and S4). As an example, the

theoretical calculations predicted that $CoCO_3$ would spontaneously react with CH_4 to produce CoO and CH_3COOH at a reaction temperature above 994 K (Fig. 1A and Fig. S4A). However, it should be noted that the spontaneity criterion alone does not guarantee the occurrence of the reaction, because the activation barriers for the elementary reaction steps during the whole reaction process were not considered in the calculation.

Thermogravimetric analysis (TGA) of the metal carbonates can provide important experimental information for predicting their CO_2 release behavior and thereby optimizing the reaction conditions. TGA measurements were carried out for commercially available metal carbonates that usually exist in partial hydroxide form, due to their high hydrophilicity (Fig. S5). Fig. 1B shows the TGA–differential scanning calorimetry (DSC) profiles of $(CoCO_3)_2 \cdot [Co(OH)_2]_3$, displaying two-step weight losses. The slight weight decrease up to 200 °C originated from the H_2O desorption while $Co(OH)_2$ transformed into CoO. A steep weight decrease was observed above 200 °C, whose corresponding DSC signal indicates the endothermic nature of the CO_2 release from $CoCO_3$ [37]. The CO_2 release continued until the temperature reached 350 °C; at this point, the releasable CO_2 was almost fully desorbed from $(CoCO_3)_2 \cdot [Co(OH)_2]_3$, which was transformed into a mixture of Co_3O_4 and CoO phases. In fact, the structural transformation was clearly evidenced by XRD, which shows that the pristine hexagonal crystal structure of $(CoCO_3)_2 \cdot [Co(OH)_2]_3$ was fully converted to cubic Co_3O_4 mixed with CoO (Fig. 1C) [37,38]. $CuCO_3 \cdot Cu(OH)_2$ and $(ZnCO_3)_2 \cdot [Zn(OH)_2]_3$ exhibited similar weight loss profiles with stepwise desorptions of H_2O and CO_2, but their weight losses and desorption temperatures were different, due to their different framework energies (Fig. S5).

The temperature dependence of the CO_2 release behavior of the metal carbonates indicates a possible route to make the reaction in Eq. 3 feasible. It is well established that supplying thermal energy increases the vibrational energy of all molecules [39]. Similarly, the vibrational energy of CO_2 in carbonate form should increase with increasing desorption temperature. Beyond the critical desorption temperature, the CO_2 molecule can be freely released from the carbonate form. Compared to CO_2 in the free molecular state, the CO_2 molecule bound as the carbonate form should be easier to activate under the same conditions, as evidenced by the different E_g values for CO_2 and CO_3^{2-} shown in Fig. S2. Accordingly, the CO_2 release from the carbonate form upon increasing the desorption temperature can be considered as an activation process for CO_2 in that form; hence, metal carbonates can be considered as a pre-activated CO_2 reservoir. To the best of our knowledge, this would be a new key approach for converting CH_4 using metal carbonates containing pre-activated CO_2 species in their carbonate structure. According to the Sabatier's principle, for a successful reaction, the reacting species should be neither strongly nor weakly bound to the surface on which the reaction occurs, and there should be a point having $\Delta G = 0$ where the adsorption and desorption of reacting species are in equilibrium [40–42]. Similarly, as the reaction temperature increases, the vibrational energy of CO_2 in the carbonate structure increases up to a maximum, at which the vibrating CO_2 can be released in the free molecular state. At this point, if CH_4 is also activated in close proximity to the vibrating CO_2, the two species can likely react as soon as CO_2 is released from the carbonate structure. Exploiting this release process of CO_2 with different temperature-dependent vibrational energies is an effective way to realize the thermodynamically favorable reaction between CH_4 and CO_2 in metal carbonates with a negative ΔG region corresponding to a spontaneous process.

3.2. CH_4 conversion to CH_3COOH using metal carbonates as the pre-activated CO_2 reservoir

Based on the phonon calculations and TGA results in Fig. 1A and B, we investigated the reaction probabilities between $(CoCO_3)_2 \cdot [Co(OH)_2]_3$ and CH_4 in a pressurized continuous flow reactor, with CH_4 gas fed at 20 bar to overcome the entropy barrier and enable the reaction in
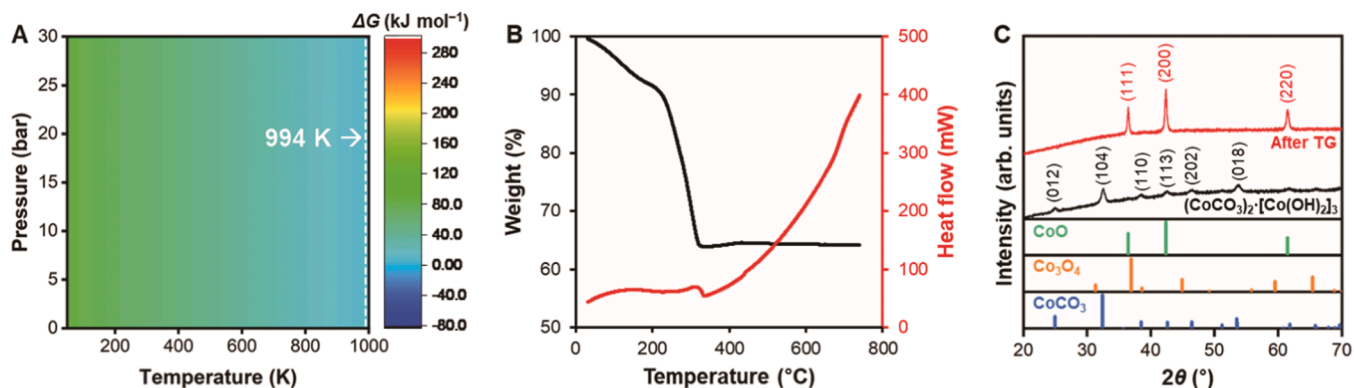
Fig. 1. (A) Color map of calculated reaction Gibbs energy (ΔG) as a function of temperature and pressure obtained using $CoCO_3$ in Eq. 3, *i.e.*, $CoCO_3$ (s) + CH_4 (g) → CoO (s) + CH_3COOH (g). (B) TGA (black) and DSC (red) profiles of cobalt carbonate basic, $(CoCO_3)_2 \cdot [Co(OH)_2]_3$ under N_2 atmosphere in a temperature range of 30–800 °C. (C) XRD patterns of cobalt carbonate basic before (black) and after TGA (red), displaying vertical (hkl) lines corresponding to $CoCO_3$ (blue), Co_3O_4 (orange), and CoO (green) obtained from the JCPDS database.

Eq. 3. Note that we prescreened the pressure effect on this reaction feasibility, and found that the high pressure with 20 bar is prerequisite for successful reaction. Higher pressure may increase the reaction performance further, but above 20 bar was not investigated in our laboratory due to the safety issue. First, the structural changes in $(CoCO_3)_2 \cdot [Co(OH)_2]_3$ and the CH_4 activation processes were investigated in the reactor under CH_4 flow and temperature control. The XRD results showed that the pristine hexagonal crystal structure of $(CoCO_3)_2 \cdot [Co(OH)_2]_3$ was changed to cubic CoO upon stepwise increasing the applied temperature from 150 to 300°C (Fig. 2A). The CO_2 release was also demonstrated by the FT-IR spectra, in which the peak at 1400 cm^{-1}, originated from the carbonate structure in $(CoCO_3)_2 \cdot [Co(OH)_2]_3$, showed a gradual decrease (orange dashed line-framed box in Fig. 2B) [43]. Compared to the transformation observed under inert gas conditions (Fig. 1C), the full transformation of $(CoCO_3)_2 \cdot [Co(OH)_2]_3$ to CoO was observed at the slightly higher temperature of 300 °C, due to the pressurized CH_4 environment. The FT-IR spectra also provided clear evidence of CH_4 activation on the surface of $(CoCO_3)_2 \cdot [Co(OH)_2]_3$, with new peaks at 2934 and 2858 cm^{-1} indicating the formation of Co–CH_3 species as the applied temperature increased (blue dashed line-framed box in Fig. 2B and corresponding magnified spectra in Fig. 2C) [44, 45]. This is consistent with the observation that the C–H bonds in CH_4 can be activated by various transition metals that form metal–methyl species [44,45]. It should be noted that the highest peak intensity was observed at 250 °C (Fig. 2C), indicating that this is the most effective temperature for CH_4 activation on $(CoCO_3)_2 \cdot [Co(OH)_2]_3$.

Fig. 2D shows a bar chart displaying the product yield of the reaction

between $(CoCO_3)_2 \cdot [Co(OH)_2]_3$ and CH_4, in which CH_3COOH was obtained as the main product without other gaseous or liquid products. (Fig. S6). As the reaction temperature increased from 150 to 300°C, the CH_3COOH yield increased dramatically, reaching the maximum at 250 °C, and then decreased at 300 °C with the formation of CH_3CHO, resulting in a clear volcano shape of the CH_3COOH yield *vs.* reaction temperature plot. The formation of CH_3CHO might be attributed to the dissociative adsorption of CO_2 to CO* and O* on the surface of metal oxide and subsequent insertion of CO* to CH_4, which is under investigation in our laboratory. The CH_3COOH yield was correlated with the CO_2 release behavior by superimposing the first-derivative curve (dw/ dT, black line profile in Fig. 2D) obtained from the TGA profile in Fig. 1B. The superimposed plots indicated that the maximum CH_3COOH yield was obtained when the first-derivative curve exhibited an upward trend. This means that the reaction was not linearly dependent on the reaction temperature, but depended on the CO_2 release behavior. The explosive production of CH_3COOH at 250 °C could be explained by the TGA (Fig. 1B), XRD (Fig. 2A), and FT-IR (Fig. 2B) results. The CO_2 release from $(CoCO_3)_2 \cdot [Co(OH)_2]_3$ started from approximately 230 °C (T_{start}) and continued up to 270 °C (T_{max}) (table S1). As shown by the FT-IR data (Figs. 2B and 2C), the CH_4 activation was facilitated at ~250 °C, that is, between the T_{start} and T_{max} values of the CO_2 release from $(CoCO_3)_2 \cdot [Co(OH)_2]_3$. Matching the CH_4 activation temperature with the temperature range of CO_2 release enabled the coupling between CH_4 and CO_2 to produce CH_3COOH.

The new reaction strategy for coupling vibrating CO_2 being released from the surface of metal carbonates with CH_4 activated on a metal
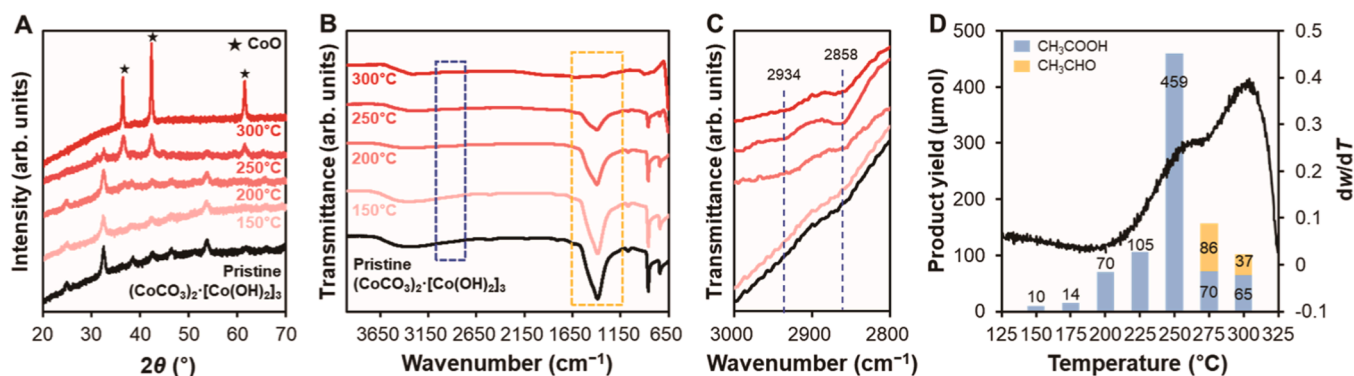
Fig. 2. (A) XRD patterns and (B) FT-IR spectra of cobalt carbonate basic after reaction under CH_4 flow at temperatures varied in the 150–300 °C range in 50 °C steps; (C) magnified view of FT-IR spectral region marked by the blue dashed line-framed box in (B). (D) Product yield (blue and yellow bars, left y-axis values) of the reaction between cobalt carbonate basic and CH_4 at temperatures varied in the 150–300 °C range in 25 °C steps, along with first-derivative plot (dw/dT, black line profile, right y-axis values) obtained from the TGA profile in Fig. 1B.

center in the metal carbonate framework can be generalized to other metal carbonates that were screened using phonon calculations (Figs. S3 and S4). $CuCO_3 \cdot Cu(OH)_2$ and $(ZnCO_3)_2 \cdot [Zn(OH)_2]_3$ exhibited similar trends in the reaction with CH_4 to produce CH_3COOH (Figs. S7 and S8). Similar to $(CoCO_3)_2 \cdot [Co(OH)_2]_3$, the CH_3COOH yields showed volcano-shaped plots with maximum yields at a specific reaction temperature, located between the T_{start} and T_{max} values (Tables S1 and S2). The CH_3COOH yields of $CuCO_3 \cdot Cu(OH)_2$ and $(ZnCO_3)_2 \cdot [Zn(OH)_2]_3$ were significantly lower than that of $(CoCO_3)_2 \cdot [Co(OH)_2]_3$, which might be attributed to their lower surface areas and intrinsic activities (Tables S1, S2 and Fig. S9). The systematic analysis of the reaction of metal carbonates under CH_4 feeding conditions showed that the metal carbonates that were predicted to spontaneously undergo the reaction in Eq. 3 based on phonon calculations (Figs. S3 and S4) could convert CH_4 to CH_3COOH by reacting with CO_2 released from the metal carbonate surface.

3.3. Sequential activation of CO_2 and CH_4 for production of CH_3COOH using metal oxides

Our ultimate goal is not only to develop a new one-way reaction pathway for converting CH_4 and CO_2 in metal carbonates (Fig. S10), but also to design a new sustainable reaction cycle for the reaction between CH_4 and CO_2 using the metal oxide as CO_2-storing starting material (Fig. 3 and Fig. S11). We prechecked the reaction between CH_4 and CO_2 under continuous co-feeding condition, and confirmed that the equimolar direct coupling between CH_4 and CO_2 was impossible due to the thermodynamic non-spontaneity as mentioned in many theoretical studies [28–30]. Starting from the substrate for CO_2 activation obtained by carbonating the surface of a metal oxide, we proposed a reaction cycle based on the scientific rationale discussed above (Fig. 3). For the CO_2 activation process, CO_2 was fed to the metal oxide, whose surface could be partially carbonated [(i) in Fig. 3]. This step is important for generating the releasable CO_2 in carbonate form on the external surface of the metal oxide. Then, the CO_2 gas was switched to CH_4 for its activation on the metal center of the metal oxide [(ii) in Fig. 3]. Based on the

FT-IR and reaction data in Fig. 2C and D, we applied the optimal predetermined temperature for the formation of metal–CH_3 species. Under CH_4 gas flow conditions, the two reactive species (i.e., the releasable CO_2 on the carbonated surface and the metal–CH_3 species) may be concentrated in close proximity, facilitating their coupling to form CH_3COOH [(iii) in Fig. 3]. Note that the adsorbed CO_2 species can be spontaneously released as the temperature raises, at which we expect that the CO_2 can be coupled to the CH_3 in the metal–CH_3 species. The continuous gas feeding condition with inert balance gas at temperatures much higher than the boiling points of the products may lead to the desorption of the final product, which can then be condensed in a cold trap placed after the reactor [(iv) in Fig. 3].

The proposed reaction cycle was realized using nanostructured Co_3O_4 (denoted as nCo_3O_4) synthesized in this laboratory as the starting metal oxide with high surface area (Fig. S12 and table S3). Our preliminary experiment demonstrated that the activity depended on the surface area, which resulted in nCo_3O_4 with higher surface area delivering a higher CH_3COOH yield than the commercially available bulk Co_3O_4 (denoted as bCo_3O_4) with lower surface area (Table S3). The proposed reaction step (i) includes CO_2 activation by feeding pressurized CO_2 to the metal oxide. Prior to this, we determined the optimal temperature for CO_2 absorption on nCo_3O_4, and 250 °C was selected as the efficient CO_2 absorption temperature, leading to carbonate formation on the surface of nCo_3O_4 (Fig. S13). The CO_2 activation step (i) resulted in an increased density of carbon atoms on the external surface of nCo_3O_4 compared to the pristine nCo_3O_4 before CO_2 treatment (Fig. 4A and B). According to the FT-IR analysis (Fig. S13A), the carbonaceous species on the external surface of nCo_3O_4 were in the carbonate form. However, the XRD patterns did not show the presence of a fully crystalline carbonate framework, indicating that the carbonate structure was formed only on the external surface of nCo_3O_4, with island-like distribution without an ordered arrangement (Fig. S13B).

For step (ii), CH_4 gas was fed at 250 °C and pressurized to 20 bar based on the experimental observation that $(CoCO_3)_2 \cdot [Co(OH)_2]_3$ exhibited the maximum CH_3COOH yield by reacting with CH_4 (Fig. 2D). When CH_4 was fed to the nCo_3O_4 material pretreated with CO_2, the density of carbon atoms increased more significantly than for the CO_2-treated nCo_3O_4 (Fig. 4C). The surface density of metal element (Co) is not observable, indicating that carbonaceous species formed a thick coating film throughout the external surface of nCo_3O_4. In steps (iii) and (iv), the activated CH_4 and CO_2 on Co metal centers and the surface of the nCo_3O_4 framework, respectively, combined to form CH_3COOH that could be desorbed during continuous gas feeding, condensed in the cold trap filled with ethanol, and accumulated as the reaction proceeded. The accumulated liquid product was analyzed by gas chromatography, which confirmed the presence of CH_3COOH as the sole product. One cycle of reaction was terminated after purging the reactor with inert gas.

The proposed reaction cycle in Fig. 3 was not clarified yet, and hence should be investigated further. In situ spectroscopic characterization tools using isotope gases and theoretical energy calculations on many possible transition and intermediate states are currently doing in this laboratory.

3.4. Sustainable carbon-consuming cycle for production of CH_3COOH using cobalt oxide

To confirm the sustainability of the process, the complete reaction cycle in Fig. 3 was repeated 12 times using nCo_3O_4. After each cycle, the reaction product was separated from the trap and identified as CH_3COOH (linear plots in Fig. 5). The results show that CH_3COOH was produced repeatedly; however, a gradual decrease in the Co_3O_4 weight-based CH_3COOH yield (μmol g_{Co3O4}^{-1}) was observed with increasing number of reaction cycles. Compared to the 1st-cycle yield (0.427 μmol g_{Co3O4}^{-1}), 36.8% and 76.1% lower yields were observed after the 7th and 12th cycles, respectively (Fig. 5). The XRD data confirmed that the peaks of nCo_3O_4 became sharper, indicating that the domain size of nCo_3O_4
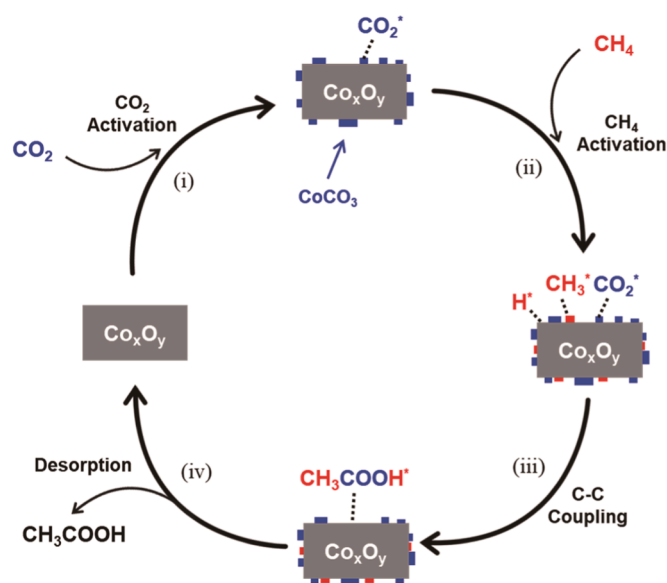
Fig. 3. Proposed reaction cycle for sequential activation of CO_2 and CH_4 to produce CH_3COOH, using cobalt oxide as starting metal oxide: (i) CO_2 activation on the surface of cobalt oxide, forming cobalt carbonate on the external surface, (ii) CH_4 activation on cobalt metal site adjacent to carbonate on the external surface of cobalt oxide, (iii) formation of CH_3COOH via C–C coupling, and (iv) desorption of CH_3COOH with regeneration of cobalt oxide as starting metal oxide, which can then participate in the new reaction cycle.
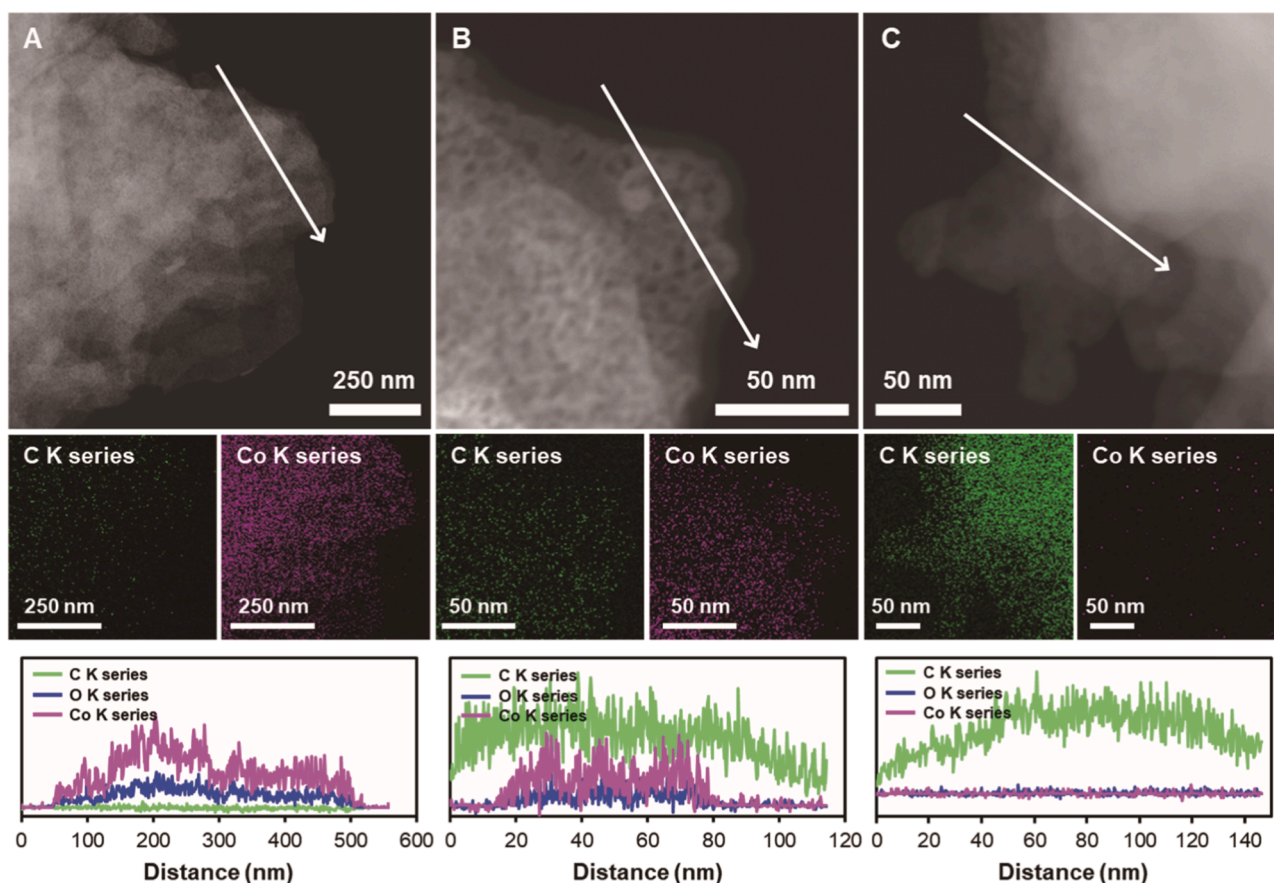
Fig. 4. TEM images (top row), corresponding TEM–EDS elemental mappings (middle row), and line scan profiles (bottom row) for C (green), O (blue), and Co (magenta) elements of (A) pristine nCo_3O_4 before CO_2 treatment, (B) nCo_3O_4 after CO_2 treatment, and (C) nCo_3O_4 after sequential CO_2/CH_4 treatment.
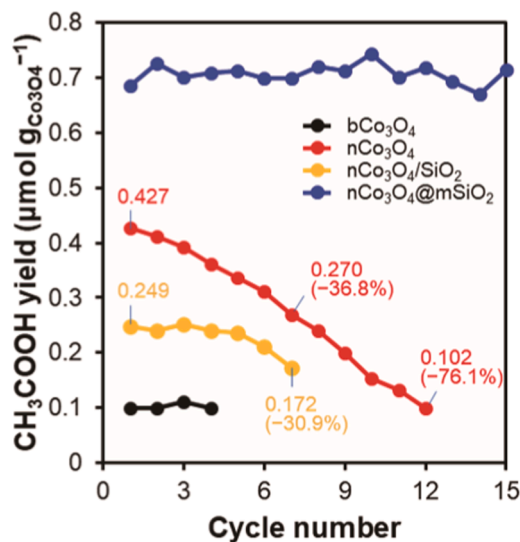
Fig. 5. Co_3O_4 weight-based CH_3COOH yields obtained using various Co_3O_4-based materials during repeated reaction cycles following Fig. 3: bCo_3O_4 (black), nCo_3O_4 (red), nCo_3O_4/SiO_2 (yellow), nCo_3O_4 @$mSiO_2$ (blue).

increased through agglomeration (Fig. S14A). This clearly indicated that nCo_3O_4 formed larger agglomerates, resulting in a lower porosity and surface area (Fig. S14B and Table S4). During the repeated CO_2 absorption processes, which formed carbonate structures on the external surface of nCo_3O_4, adjacent Co_3O_4 particles could adhere to each other,

leading to agglomeration (Figs. S14C and S14D), which resulted in a decreased surface area and thus a lower CH_3COOH yield (Table S4). However, this adhesion issue was partially resolved by diluting nCo_3O_4 with silica powder (sample denoted as nCo_3O_4/SiO_2 in Fig. 5). Using nCo_3O_4/SiO_2, the CH_3COOH yield after the 1st cycle decreased by 30.9% after the 7th cycle, whereas with bare nCo_3O_4 the 1st-cycle CH_3COOH yield decreased by 36.8% after the 7th cycle (Fig. 5). The physical distancing between nCo_3O_4 particles created by the introduction of silica prevented their agglomeration by adhesion during the CO_2 absorption process [(i) in Fig. 3].

We further resolved the agglomeration issue of nCo_3O_4 by synthesizing silica shell-coated core@shell-type $nCo_3O_4@mSiO_2$ with nanosponge-like aggregates (Fig. 6). Small Co_3O_4 nanoparticles with a mean size of 15 nm were successfully encapsulated by a SiO_2 shell with mesoporous structure, forming nanosponge-like aggregates (Fig. 6C). The SiO_2 shell of $nCo_3O_4@mSiO_2$ possessed a molecule-accessible mesoporous channel with average diameter of 2.5 nm and surface area of 751 m^2 g^{-1} (Table S4). No physically separated mesoporous SiO_2 phase was observed in the TEM image (Fig. 6C). When the $nCo_3O_4@mSiO_2$ was applied during the sequential activation of CO_2/CH_4, 140 μmol of CO_2 were chemisorbed on the 1 g of $nCo_3O_4@mSiO_2$, from which 0.151 μmol of CH_3COOH was produced. The $nCo_3O_4@mSiO_2$ exhibited an approximately 1.6 times higher CH_3COOH yield than nCo_3O_4 in the 1st reaction cycle (Fig. 5 and Table S4), which might be attributed to the high surface area of the 15 nm-sized Co_3O_4 nanoparticles. More surprisingly, $nCo_3O_4@mSiO_2$ exhibited a stable reaction performance, without a decrease in CH_3COOH yield during 15 reaction cycles (Fig. 5). The Co_3O_4 weight-based CH_3COOH yield after the 1st cycle was almost unchanged, and no significant restructuring in $nCo_3O_4@mSiO_2$ was observed in XRD and TEM analyses (Fig. 6). It
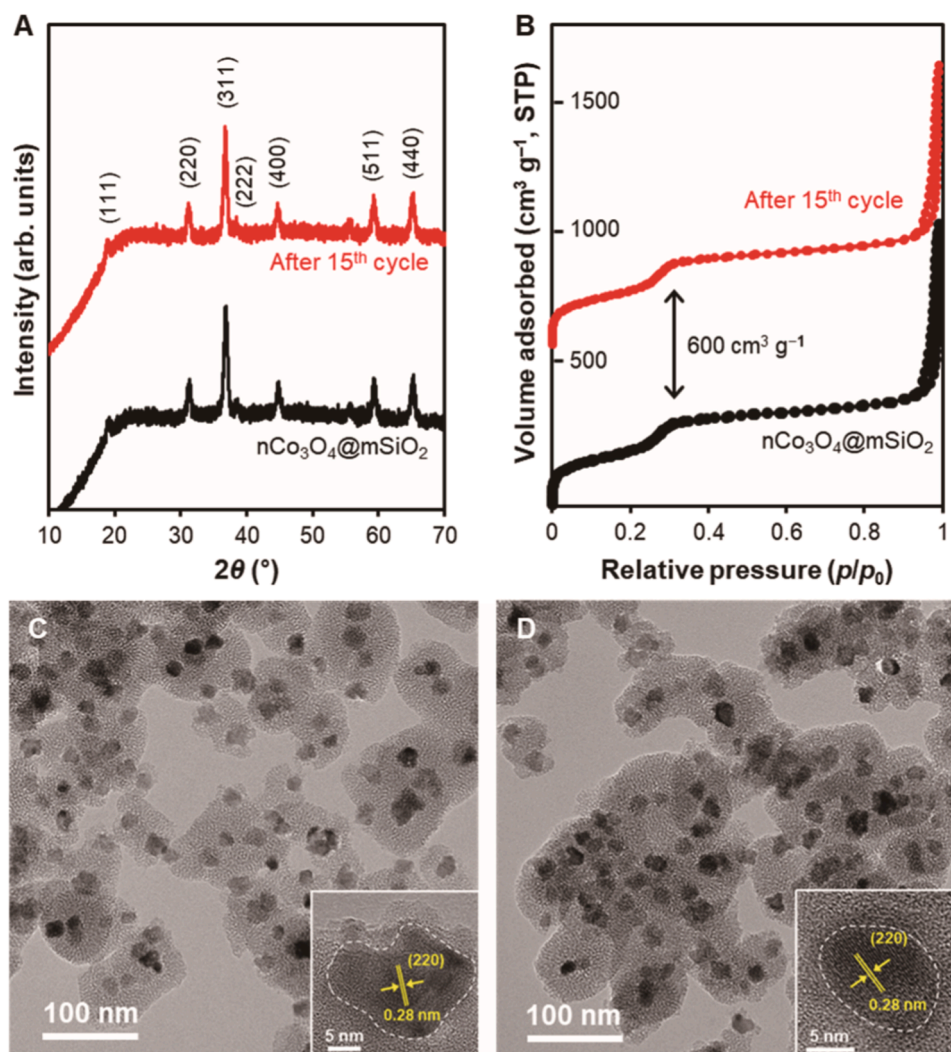
Fig. 6. (A) XRD patterns and (B) N_2 adsorption/desorption isotherm of fresh $nCo_3O_4@SiO_2$ sample before reaction (black) and after 15th reaction cycle in Fig. 3 (red). TEM images of (C) fresh $nCo_3O_4@SiO_2$ sample before reaction and (D) $nCo_3O_4@SiO_2$ after 15th reaction cycle, with inset images showing (220) lattice fringes of Co_3O_4 nanoparticles encapsulated by SiO_2 shell.

should be noted that the bare nCo_3O_4 exhibited a 76.1% loss in CH_3COOH yield after the 12th cycle (Fig. 5). The encapsulation of Co_3O_4 nanoparticles by the SiO_2 shell to form a nanosponge-like architecture created a permanent physical distancing between the nanoparticles, which prevented their agglomeration and finally maintained the sustainable effect of the Co_3O_4 nanoparticles in the production of CH_3COOH during repeated cycles. Although the reaction was not further repeated beyond the 15th cycle, the observation that the pristine structure of $nCo_3O_4@mSiO_2$ was fully maintained should guarantee the repeatability of the process over further cycles.

4. Conclusion

In conclusion, a new reaction cycle consisting of stepwise CO_2 and CH_4 activations to produce CH_3COOH has been developed using naturally abundant metal oxides. The equimolar reaction between CO_2 and CH_4 in the free molecular state is non-spontaneous; this problem was solved by reacting CH_4 with the carbonate species in Co-, Cu-, and Zn-based metal carbonates that were selected based on theoretical calculations. Although the bare nCo_3O_4 made the proposed reaction cycle feasible, the CO_2 absorption step induced adhesion of nCo_3O_4 particles, with subsequent agglomeration. However, we synthesized Co_3O_4 nanoparticles encapsulated in a core@shell structure coated with a mesoporous silica shell (*i.e.*, $nCo_3O_4@mSiO_2$), in which the Co_3O_4 nanoparticles were in physical distancing between the interconnected mesoporous channels of the silica framework. As a consequence, the $nCo_3O_4@mSiO_2$ structure unraveled the last puzzle to complete the sustainable carbon-consuming cycle. The new concept based on the stepwise activation of CO_2 and CH_4 can be further generalized to various metal oxides, opening a new avenue toward sustainable carbon-consuming chemical processes.

CRediT authorship contribution statement

Seungdon Kwon: Investigation, Experiments, Writing – review & editing. **Hyogeun Yang**: Experiments, Writing – review & editing. **Youngjae Yu**: Experiments, Writing – review & editing. **Yuyeol Choi**: Experiments, Theoretical calculations, Writing – review & editing. **Nagyeong Kim**: Experiments. **Gye Hong Kim**: Theoretical calculations, Writing – review & editing. **Kyoung Chul Ko**: Theoretical calculations,

Writing – original draft for Theoretical calculations part, Writing – review & editing. **Kyungsu Na**: Conceptualization, Supervision, Project administration, Investigation, Theoretical calculations, Writing – original draft, Writing – review & editing.

Declaration of Competing Interest

The authors declare no competing financial interest.

Data Availability

No data was used for the research described in the article. All data are available in the main text or the supplementary material.

Acknowledgments

Appendix A. Supporting information

Supplementary data associated with this article can be found in the online version at doi:10.1016/j.apcatb.2023.123120.

References

[1] S.J. Davis, N.S. Lewis, M. Shaner, S. Aggarwal, D. Arent, I.L. Azevedo, S.M. Benson, T. Bradley, J. Brouwer, Y. Chiang, C.T.M. Clack, A. Cohen, S. Doig, J. Edmonds, P. Fennell, C.B. Field, B. Hannegan, B. Hodge, M.I. Hoffert, E. Ingersoll, P. Jaramillo, K.S. Lackner, K.J. Mach, M. Mastrandrea, J. Ogden, P.F. Peterson, D. L. Sanchez, D. Sperling, J. Stagner, J.E. Trancik, C. Yang, K. Caldeira, Net-zero emissions energy systems, Science 360 (2018) eaas9793.

[2] C. Hepburn, E. Adlen, J. Beddington, E.A. Carter, S. Fuss, N.M. Dowell, J.C. Minx, P. Smith, C.K. Williams, The technological and economic prospects for CO_2 utilization and removal, Nature 575 (2019) 87–97.

[3] R.S. Haszeldine, Carbon capture and storage: how green can black be? Science 325 (2009) 1647–1652.

[4] S.Ó. Snæbjörnsdóttir, B. Sigfússon, C. Marieni, D. Goldberg, S.R. Gislason, E. H. Oelkers, Carbon dioxide storage through mineral carbonation, Nat. Rev. Earth Environ. 1 (2020) 90–102.

[5] A. Sanna, M. Uibu, G. Caramanna, R. Kuusik, M.M. Maroto-Valer, A review of mineral carbonation technologies to sequester CO_2, Chem. Soc. Rev. 43 (2014) 8049–8080.

[6] Y. Kim, Y. Song, Y. Kim, K. Na, Multifunctional long-lived catalysts for direct hydrogenative conversion of CO_2 to liquid hydrocarbons with upscaling C_{5+} productivity, J. Mater. Chem. A 10 (2022) 21862–21873.

[7] C. Chen, X. Zhu, X. Wen, Y. Zhou, L. Zhou, H. Li, L. Tao, Q. Li, S. Du, T. Liu, D. Yan, C. Xie, Y. Zou, Y. Wang, R. Chen, J. Huo, Y. Li, J. Cheng, H. Su, X. Zhao, W. Cheng, Q. Liu, H. Lin, J. Luo, J. Chen, M. Dong, K. Cheng, C. Li, S. Wang, Coupling N_2 and CO_2 in H_2O to synthesize urea under ambient conditions, Nat. Chem. 12 (2020) 717–724.

[8] S. Jin, Z. Hao, K. Zhang, Z. Yan, J. Chen, Advances and challenges for the electrochemical reduction of CO_2 to CO: from fundamentals to industrialization, Angew. Chem. 133 (2021) 20627–20648.

[9] S. Kattel, P.J. Ramírez, J.G. Chen, J.A. Rodriguez, P. Liu, Active sites for CO_2 hydrogenation to methanol on Cu/ZnO catalysts, Science 355 (2017) 1296–1299.

[10] S. Moret, P.J. Dyson, G. Laurenczy, Direct synthesis of formic acid from carbon dioxide by hydrogenation in acidic media, Nat. Commun. 5 (2014) 4017.

[11] S.C. Peter, Reduction of CO_2 to chemicals and fuels: a solution to global warming and energy crisis, ACS Energy Lett. 3 (2018) 1557–1561.

[12] S. Fukuoka, M. Kawamura, K. Komiya, M. Tojo, H. Hachiya, K. Hasegawa, M. Aminaka, H. Okamoto, I. Fukawa, S. Konno, A novel non-phosgene polycarbonate production process using by-product CO_2 as starting material, Green. Chem. 5 (2003) 497–507.

[13] S. Inoue, H. Koinuma, T. Tsuruta, Copolymerization of carbon dioxide and epoxide, J. Polym. Sci. B Polym. Lett. 7 (1969) 287–292.

[14] R.R. Shaikh, S. Pornpraprom, V. D`Elia, Catalytic strategies for the cycloaddition of pure, diluted, and waste CO_2 to epoxides under ambient conditions, ACS Catal. 8 (2018) 419–450.

[15] X. Lim, How to make the most of carbon dioxide, Nature 526 (2015) 628–631.

[16] N. Feng, H. Lin, H. Song, L. Yang, D. Tang, F. Deng, J. Ye, Efficient and selective photocatalytic CH_4 conversion to CH_3OH with O_2 by controlling overoxidation on TiO_2, Nat. Commun. 12 (2021) 4652.

[17] K.T. Dinh, M.M. Sullivan, P. Serna, R.J. Meyer, Y. Roman-Leshkov, Breaking the selectivity-conversion limit of partial methane oxidation with tandem heterogeneous catalysts, ACS Catal. 11 (2021) 9262–9270.

[18] Y. Kwon, T.Y. Kim, G. Kwon, J. Yi, H. Lee, Selective activation of methane on single-atom catalyst of rhodium dispersed on zirconia for direct conversion, J. Am. Chem. Soc. 139 (2017) 17694–17699.

[19] J. Si, G. Zhao, W. Sun, J. Liu, C. Guan, Y. Yang, X. Shi, Y. Lu, Oxidative coupling of methane: examining the inactivity of the MnO_x-Na_2WO_4/SiO_2 catalyst at low temperature, Angew. Chem. 134 (2022), e202117201.

[20] L. Sun, Y. Wang, N. Guan, L. Li, Methane activation and utilization: current status and future challenges, Energy Technol. 8 (2020), 1900826.

[21] J. Mouawad, 2009. Estimate places natural gas reserves 35% higher, New York Times, 2009.

[22] R.W. Howarth, A. Ingraffea, T. Engelder, Should fracking stop? Nature 477 (2011) 271–275.

[23] E. McFarland, Unconventional chemistry for unconventional natural gas, Science 338 (2012) 340–342.

[24] Á. López-Martín, A. Caballero, G. Colón, Unraveling the Mo/HZSM-5 reduction pre-treatment effect on methane dehydroaromatization reaction, Appl. Catal. B 312 (2022), 121382.

[25] Y. Choi, S. Park, S. Kwon, K.C. Ko, K. Na, Controlled electropositive catalytic sites on zeolites for achieving high CH_3Cl selectivity via electrophilic CH_4 chlorination using Cl_2, J. Mater. Chem. A 10 (2022) 24475–24486.

[26] Y. Song, E. Ozdemir, S. Ramesh, A. Adishev, S. Subramanian, A. Harale, M. Albuali, B.A. Fadhel, A. Jamal, D. Moon, S.H. Choi, C.T. Yavuz, Dry reforming of methane by stable Ni–Mo nanocatalysts on single-crystalline MgO, Science 367 (2020) 777–781.

[27] R. Shavi, J. Ko, A. Cho, J.W. Han, J.G. Seo, Mechanistic insight into the quantitative synthesis of acetic acid by direct conversion of CH_4 and CO_2: an experimental and theoretical approach, Appl. Catal. B 229 (2018) 237–248.

[28] Y. Zhao, Q. Cui, J. Han, H. Wang, X. Zhu, Q. Ge, Direct C–C coupling of CO_2 and the methyl group from CH_4 activation through facile insertion of CO_2 into Zn–CH_3 σ-bond, J. Am. Chem. Soc. 138 (2016) 10191–10198.

[29] A.M. Rabie, M.A. Betiha, S. Park, Direct synthesis of acetic acid by simultaneous co-activation of methane and CO_2 over Cu-exchanged ZSM-5 catalysts, Appl. Catal. B 215 (2017) 50–59.

[30] C. Tu, X. Nie, J.G. Chen, Insight into acetic acid synthesis from the reaction of CH_4 and CO_2, ACS Catal. 11 (2021) 3384–3401.

[31] A. Haynes, P.M. Maitlis, G.E. Morris, G.J. Sunley, H. Adams, P.W. Badger, C. M. Bowers, D.B. Cook, P.I.P. Elliott, T. Ghaffar, H. Green, T.R. Griffin, M. Payne, J. M. Pearson, M.J. Taylor, P.W. Vickers, R.J. Watt, Promotion of iridium-catalyzed methanol carbonylation: mechanistic studies of the cativa process, J. Am. Chem. Soc. 126 (2004) 2847–2861.

[32] F.E. Paulik, J.F. Roth, Novel catalysts for the low-pressure carbonylation of methanol to acetic acid, Chem. Commun. (Lond.) 24 (1968) 1578a–1578a.

[33] M.J. Howard, G.J. Sunley, A.D. Poole, R.J. Watt, B.K. Sharma, New acetyls techonologies from BP chemicals, Stud. Surf. Sci. Catal. 121 (1999) 61–68.

[34] V. Blum, R. Gehrke, F. Hanke, P. Havu, V. Havu, X. Ren, K. Reuter, M. Scheffler, Ab initio molecular simulations with numeric atom-centered orbitals, Comput. Phys. Commun. 180 (2009) 2175–2196.

[35] J. Ilsemann, A. Straß-Eifert, J. Friedland, L. Kiewidt, J. Thöming, M. Bäumer, R. Güttel, Cobalt@silica core-shell catalysts for hydrogenation of CO/CO_2 mixtures to methane, ChemCatChem 11 (2019) 4884–4893.

[36] S. Lee, J. Noh, S. Hong, Y.K. Kim, J. Jang, Dual stimuli-responsive smart fluid of graphene oxide-coated iron oxide/silica core/shell nanoparticles, Chem. Mater. 28 (2016) 2624–2633.

[37] M. Nassar, I. Ahmed, Hydrothermal synthesis of cobalt carbonates using different counter ions: an efficient precursor to nano-sized cobalt oxide (Co_3O_4), Polyhedron 30 (2011) 2431–2437.

[38] M. Oza, D. Kanchan, J. Joshi, M. Joshi, Structural, DFT, vibrational spectroscopic, thermal, electrical and magnetic characterizations of hydrothermally grown $CoCO_3$ microcrystals, J. Mater. Sci.: Mater. Electron 31 (2020) 10177–10185.

[39] P.M.A. Sherwood, Vibrational Spectroscopy of Solids, Cambridge University Press, 2011.

[40] S. Hu, W.-X. Li, Sabatier principle of metal-support interaction for design of ultrastable metal nanocatalysts, Science 374 (2021) 1360–1365.

[41] A.J. Medford, A. Vojvodic, J.S. Hummelshøj, J. Voss, F. Abild-Pedersen, F. Studt, T. Bligaard, A. Nilsson, J.K. Nørskov, From the Sabatier principle to a predictive theory of transition-metal heterogeneous catalysis, J. Catal. 328 (2015) 36–42.

[42] R. Inoue, S. Ueda, K. Wakuta, K. Sasaki, T. Ariyama, Thermodynamic consideration on the absorption properties of carbon dioxide to basic oxide, ISIJ Int. 50 (2010) 1532–1538.

[43] R. Xu, H.C. Zeng, Dimensional control of cobalt-hydroxide-carbonate nanorods and their thermal conversion to one-dimensional arrays of Co_3O_4 nanoparticles, J. Phys. Chem. B 107 (2003) 12643–12649.

[44] X. Yu, V. De Waele, A. Löfberg, V. Ordomsky, A.Y. Khodakov, Selective photocatalytic conversion of methane into carbon monoxide over zinc-heteropolyacid-titania nanocomposites, Nat. Commun. 10 (2019) 700.

[45] L. Azancot, L.F. Bobadilla, M.A. Centeno, J.A. Odriozola, IR spectroscopic insights into the coking-resistance effect of potassium on nickel-based catalyst during dry reforming of methane, Appl. Catal. B 285 (2021), 119822.